Title

Climate change impact on residual contaminants under sustainable remediation

Authors

Libera, Arianna

de Barros, Felipe PJ

Faybishenko, Boris

et al.

Publication Date

2019-10-01

DOI

10.1016/j.jconhyd.2019.103518

Peer reviewed

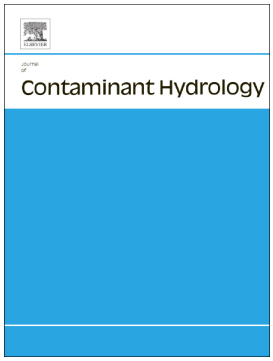

Climate change impact on residual contaminants under sustainable remediation

Arianna Libera, Felipe P.J. de Barros, Boris Faybishenko, Carol Eddy-Dilek, Miles Denham, Konstantin Lipnikov, David Moulton, Barbara Maco, Haruko Wainwright

PII: S0169-7722(19)30085-3
DOI: https://doi.org/10.1016/j.jconhyd.2019.103518
Article Number: 103518
Reference: CONHYD 103518

To appear in: *Journal of Contaminant Hydrology*

Received date: 22 March 2019
Revised date: 17 June 2019
Accepted date: 25 June 2019

Please cite this article as: A. Libera, F.P.J. de Barros, B. Faybishenko, et al., Climate change impact on residual contaminants under sustainable remediation, Journal of Contaminant Hydrology, https://doi.org/10.1016/j.jconhyd.2019.103518

Climate change impact on residual contaminants under sustainable remediation

Arianna Libera
Sonny Astani Dept. of Civil and Environmental Engineering
University of Southern California
Los Angeles, California, USA

Felipe P. J. de Barros
Sonny Astani Dept. of Civil and Environmental Engineering
University of Southern California
Los Angeles, California, USA

Boris Faybishenko
Lawrence Berkeley National Laboratory
Berkeley, CA, USA

Carol Eddy-Dilek
Savannah River National Laboratory
Aiken, SC, USA

Miles Denham
Panoramic Environmental Consulting, LLC
Aiken, SC, USA

Konstantin Lipnikov
Los Alamos National Laboratory
Los Alamos, NM, USA

David Moulton

Los Alamos National Laboratory
Los Alamos, NM, USA

Barbara Maco
Wactor & Wick LLP Environmental Lawyers
Oakland, CA, USA

Haruko Wainwright
Lawrence Berkeley National Laboratory
Berkeley, CA, USA

Abstract

This study investigates the potential impact of climate change on residual contaminants in vadose zones and groundwater. We assume that the effect of climate changes can be represented by perturbations in the natural recharge through the aquifer system. We perform numerical modeling of unsaturated/saturated flow and transport and consider different performance metrics: contaminant concentrations at observation wells and contaminant export at the site's boundary. We evaluate the effect of increasing and decreasing recharge as well as the impact of potential failure of surface capping structures employed to immobilize vadose zone contaminants. Our approach is demonstrated in a real case study by simulating transport of non-reactive radioactive tritium at the U.S. Department of Energy's Savannah River Site. Results show that recharge changes significantly affect well concentrations: after an initial slight dilution we identify a significant concentration increase at different observation wells some years after the recharge increase and/or the cap failure, as a consequence of contaminants' mobilization. This effect is generally emphasized and occurs earlier as the recharge increases. Under decreased aquifers' recharge the concentration could slightly increase for some years, due to a decrease of dilution, depending on the magnitude of the negative recharge shift. We identify trigger levels of recharge above which the concentration/export breakthrough curves and the time of exceedance of the Maximum Contaminant Level for tritium are remarkably affected. Moreover, we observe that the contaminant export at the control plane, identified as the risk pathway to the downgradient

population, may only be minimally affected by shifts in the natural recharge regime, except for some extreme cases. We conclude that more frequent sampling and in-situ monitoring near the source zone should be adopted to better explain concentrations' anomalies under changing climatic conditions. Moreover, the maintenance of the cap is critical not only to sequester residual contaminants in the vadose zone, but also to reduce the uncertainty associated with future precipitation changes. Finally, realistic flow and transport simulations achieved through proper calibration processes, rather than conservative modeling, should be adopted to identify non-trivial trade-offs which enable better allocation of resources towards reducing uncertainty in decision making.

1 Introduction

Subsurface contamination is recognized as a critical issue in many communities. There are more than a thousand Superfund sites in the U.S. categorized under the U.S. Environmental Protection Agency (EPA), which present large plumes of organic solvents, heavy metals and radionuclides (US Environmental Protection Agency, https://www.epa.gov/superfund). In addition, the EPA estimated the presence of more than 450,000 brownfields in the U.S., contaminated by hazardous substances, pollutants or contaminants (US Environmental Protection Agency, https://www.epa.gov/brownfields).

The practice of soil and groundwater remediation has been changing in recent decades, transitioning from intense soil removal and active treatment solutions towards passive remediation techniques such as enhanced biodegradation or monitored natural attenuation (Ellis and Hadley, 2009). The latter less-intensive remediation approaches, often identified as *sustainable remediation* techniques, have been recognized as more advantageous since they can reduce negative side effects that often accompany intensive remediation (e.g., ecological disturbance, construction noise/traffic, intensive energy use and emissions of greenhouse gases). Additionally, sustainable remediation is coupled with more innovative and attractive end-use scenarios with restricted subsurface use and longer institutional control. In most cases, a portion of contaminants are sequestered in the subsurface for a long period of time, while natural or enhanced biogeochemical processes occur to reduce contaminant concentrations. Within this context, it is critical to assess the long-term stability of residual contaminants subject to sustainable remediation

practices and to ensure that the latter will not pose significant environmental and human health risk.

Recently, O'Connell and Hou (2015a) raised the concern that climate change may pose a major risk in environmental remediation; especially with regard to the fate of residual contaminants under sustainable remediation. A hydrological shift has been identified as one of the key drivers influencing such risk and uncertainty. In changing climate, precipitation regimes (including amount and timing) are expected to change significantly, and extreme events, such as heavy rains and prolonged droughts, could become more frequent. Climate models also predict increasing temperatures, which would affect water budgets and reduce infiltration due to increased evapotranspiration. These climatic changes are occurring while groundwater is becoming increasingly important for drinking and irrigation purposes (Famiglietti, 2014).

Despite the critical need to evaluate risks associated with climate change, there is only a limited number of studies that address the effects of climate change on contaminant transport and environmental remediation. While the impact of climate change has been investigated extensively from the perspective of water resources (Gellens and Roulin, 1998; Green et al., 2011; Middelkoop et al., 2001; Pfister et al., 2004), a limited number of studies have addressed water quality issues (Visser et al., 2012). Moreover, most literature focuses on surface water (Wilby et al., 2006; Van Vliet and Zwolsman, 2008; Van Bokhoven, 2006; Futter et al., 2009; Schiedek et al., 2007), due to its visibility and accessibility (Green et al., 2011), while the studies on groundwater are mostly focused on agricultural effluents at the regional scale (Bloomfield et al., 2006; Futter et al., 2009; Li and Merchant, 2013; Olesen et al., 2007; Sjoeng et al., 2009; Whitehead et al., 2009; Wilby et al., 2006; Darracq et al., 2005; Destouni and Darracq, 2009; Park et al., 2010). Current literature lacks site-scale hydrological studies that can guide sustainable remediation under changing climate conditions within risk and performance assessments as well as within regulatory frameworks.

This study aims at evaluating the effects of climate-driven hydrological shifts on residual contaminants in vadose zones and groundwater under sustainable remediation. We simulate groundwater flow and contaminant transport through unsaturated and saturated domains. We assume that the effect of changing precipitation and temperature can be represented by perturbations/shifts of natural recharge through the aquifer system. The impacts are evaluated on the basis of different decision metrics relevant to public health risk, regulatory compliance and site

closure such as contaminant concentrations at monitoring wells and exports from site boundaries. We demonstrate our approach at the Department of Energy (DOE)'s Savannah River Site (SRS) F-Area Seepage Basins, South Carolina (SC), USA, where soil and groundwater were contaminated by various metals and radioactive contaminants during the Cold War Era. For brevity, the F-Area Seepage Basins are referred to hereafter as just F-Area. Extensive subsurface characterization and dataset at the SRS F-Area, including hundreds of wells, geophysics data and various hydrological tests, enabled the development of a subsurface model that can be considered as a testbed for flow and transport studies (Flach, 2004; Bea et al., 2013; Sassen et al., 2012; Wainwright et al., 2014; Dai et al., 2002). The SRS hence provides a unique opportunity to investigate the potential consequences of climate change on residual contamination in realistic settings that display multiple representative features of other polluted sites.

2 Background

2.1 Conceptual model

We consider a general conceptual hydrological model of a contaminated site characterized by residual contamination in the vadose zone and groundwater (Figure 1). This model extends to the SRS F-Area (Bea et al., 2013), the description of which is provided in Section 2.2. Initially, contaminants are discharged through a seepage basin located on the top of the model domain. The contaminant plume migrates vertically through the vadose zone, and laterally downgradient in the aquifer. At some sites, the plume reaches surface water bodies (e.g., a creek or a river) located close to the site boundary, through water seepage. In order to reduce contaminant migration through the vadose zone, the contaminant source zone (i.e., seepage basin) is often capped with low-permeability material, such as clay or silt. However, residual contaminants located in the vadose zone could become a persistent contaminant source to the groundwater plume (Zachara et al., 2013), as shown in Figure 1.

Figure 1: Schematic illustration of the hydrological conceptual model under investigation, representing a vertical two-dimensional cross-section driven along the middle line of the contaminant source zone.

Contaminant concentrations are typically measured at groundwater monitoring wells to ensure the plume stability and to meet the regulatory compliance. The number of wells and frequency of sampling (e.g., quarterly or annually) are determined in agreement with a regulatory agency (e.g., the EPA). Concentrations are often compared to the Maximum Contaminant Level (MCL) recommended by the EPA. Predicting the time of exceedance of MCL, for example, is an important Environmental Performance Metric (EPM) to plan the site closure or site transfer (Denham and Eddy-Dilek, 2017). In parallel, risk (and/or performance) assessments consider a variety of metrics and pathways, including contaminant mass flux/export at control planes (CPs), e.g., site boundaries, creeks or rivers (Maxwell and Kastenberg, 1999; de Barros and Rubin, 2008; de Barros et al., 2009; 2012; Atchley et al., 2013). On-site concentrations are often used to evaluate human health risk doses through direct ingestion/drinking pathways, while the export at CPs are employed to quantify risk of the downgradient population.

The changes in precipitation and temperature associated with climate change are expected to affect contaminant plumes in groundwater systems and residual contaminants in the vadose zone in a complex manner. This impact can be evaluated by considering a perturbation/shift of the natural recharge through an aquifer in a long or short time frame (O'Connell and Hou, 2015b). For example, an increase in precipitation results in higher aquifer recharge, while a decrease in precipitation, or higher temperature, hence increased evapotranspiration, leads to lower aquifer recharge. Higher recharge then (1) increases vadose-zone flow, which mobilizes sequestered contaminants, (2) raises the groundwater table and increases hydraulic gradients, resulting in enhanced plume mobility in groundwater, and (3) enhances mixing of the plume with clean water, which leads to higher dilution. On the other hand, a decrease of recharge has opposite effects, i.e, decreases the plume mobility while reducing mixing and dilution. The impact of climate change-driven altered recharge rates on different decision and performance metrics relevant to environmental remediation could potentially create trade-offs that should be quantitatively evaluated.

2.2 F-Area site description

The SRS is located in South-central South Carolina, USA, approximately 100 mi (i.e., 161 km) away from the Atlantic Ocean and occupies an area of about 800 km^2. The site was used to produce nuclear materials such as plutonium and tritium (^3H), for nuclear weapons during the

Cold War Era. The F-Area, located in the north-central part of the SRS, included three unlined discharge basins: F-1, F-2 and F-3 (Bea et al., 2013). The basins received approximately 7.1 billion liters of acidic, low-level radioactive waste solutions from processing irradiated uranium between 1955 and 1988 (Flach et al., 2004; Killian et al., 1986). The waste solution presented various radionuclides such as uranium isotopes, ^{90}Sr, ^{129}I and ^{99}Tc, among which ^{3}H, is the largest dose contributor. After the waste discharge operation was terminated in 1988, the F-Area basins were closed and capped with low-permeability material (Bea et al., 2013). Currently, an acidic contaminant plume extends from the basins approximately 600 m downgradient to the groundwater seepage near the Fourmile Branch (Bea et al., 2013). Enhanced natural attenuation is currently under way using a funnel-and-gate system which consists of groundwater flow barriers to decrease the groundwater gradient, and base injection to neutralize pH and to immobilize uranium (Tokunaga et al., 2012).

Hydrogeology at this site has been characterized extensively in many studies (Flach et al., 2004; Bea et al., 2013; Sassen et al., 2012; Wainwright et al., 2014). There are three hydrostratigraphic units within the Upper Three Runs Aquifer: an Upper Aquifer zone (UUTRA), a Tan Clay Confining Zone (TCCZ), and a Lower Aquifer zone (LUTRA). The UUTRA and LUTRA are mainly composed by clean sand, while the TCCZ is a low-permeable mixed sand-and-clay layer. The piezometric head measurements indicate that the UUTRA and LUTRA units are hydrologically connected. The bottom of the LUTRA consists of a competent clay layer confining unit, the continuous Gordon Confining (GC) unit, which separates the deeper aquifer (Gordon Aquifer) from the upper two units. The historical monitoring data collected at the SRS have shown that the contaminant plume migrates within the UUTRA and LUTRA (Sassen et al., 2012).

3 Methodology

3.1 Flow and transport simulations

We employ the two-dimensional (2D) flow and transport model adopted in Bea et al. (2013), i.e., a 2D domain approximately 2600 m long and 100 m deep along the groundwater flow line, passing through the middle of the F-3 basin of the SRS. This model has been calibrated and verified using site data (Bea et al., 2013). Figure 2 illustrates the 2D cross-section model domain.

Hydrostratigraphic Unit	Porosity ϕ [–]	Permeability k [m^2]	α [kg^{-1} $m\,s^2$]	n [–]	m [–]	S_{rl} [–]	p [–]
UUTRA	0.39	5×10^{-12}	4×10^{-4}	2	0.5	0.18	1
TCCZ	0.39	1.98×10^{-14}	5.1×10^{-5}	2	0.5	0.39	1
LUTRA	0.39	5×10^{-12}	5.1×10^{-5}	2	0.5	0.41	1

Table 1: Parameters adopted in the numerical model presented in this study. The table reports values for porosity (ϕ [–]), permeability (k [m^2]), water retention-curve parameters (α [kg^{-1} $m\,s^2$], n [–], m [–]), residual liquid pore saturation (S_{rl} [–]), Mualem (1976) parameter (p [–]) (for details, see Bea et al., 2013).

The model includes the vadose zone and three hydrostratigraphic units (i.e., UUTRA, LUTRA and TCCZ) defined in Section 2.2. We assume homogeneous average hydrogeological properties within each unit (see Table 1), whose values are compiled from available site investigation reports. Table 1 specifies porosity, permeability and capillary pressure/saturation data for the vadose zone (Flach et al., 2004; Phifer et al., 2006; Bea et al., 2013). Please refer to Appendix A of Bea et al. (2013) for the parameters description. The system is considered to be advective dominated, therefore mechanical dispersion and molecular diffusion transport processes are neglected. We simulate simple ^3H decay with a half-life of 12.3 years. No-flow boundary conditions are assigned along the two vertical sides of the 2D-cross section (see Figure 2) according to the groundwater divides (Flach, 2004; Bea et al., 2013). An impervious flow boundary condition (i.e. no-flow) is set at the bottom of the computational domain, since the confining unit at this location is highly clayey and continuous (Bea et al., 2013).

Figure 2: Two-dimensional model domain adopted in our study.

Groundwater flow and contaminant transport are simulated by means of the numerical code Amanzi which describes coupled vadose zone and groundwater flow as well as reactive transport (Freshley et al., 2012; Bea et al., 2013; Wainwright et al., 2015; Wainwright et al., 2016). Amanzi uses the mimetic finite difference method for the Richards equation and dispersion

operators, which preserves fundamental mathematical and physical properties in discrete schemes (da Veiga et al., 2014). To discretize the advection operator, it uses monotone first-order and second-order MUSCL schemes with new limiters that improve accuracy on unstructured meshes (Lipnikov et al., 2010). Amanzi has been benchmarked against other flow and transport models as well as analytical solutions for a wide range of hydrological problems.

We perform numerical simulations within the time frame 1955-2100, i.e., from the beginning of the discharge operation at the SRS. Our model is discretized into 164160 cells and we adopt a longitudinal mesh spatial resolution of 1.25 m and a variable vertical spatial resolution, with a maximum value of 2 m. A steady-state simulation is carried out to establish the groundwater table with a given recharge value at the top of the modeled domain of 4.74×10^{-6} mm/s (i.e., 150 mm/yr) before 1955. This value represents the estimated recharge based on the rainfall records and runoff estimations (Flach et al., 2004), which is kept constant over the entire domain for all the simulation timeframe, except for the discharge basin. After 1955, we perform transient simulations employing a constant ^{3}H discharge value at the seepage basin between 1955 and 1988. The average ^{3}H concentration and mass discharge rate are respectively 2.17×10^{-9} mol/kgw and around 1.11×10^{-4} mm/s, as in Bea et al. (2013). These values coincide with the average ^{3}H concentration and discharge rate of historical data between 1955 and 1988 (see Table 8 of Bea et al. (2013)). After the basin is capped in 1988, the recharge through the basin is assumed to be three-order of magnitude lower than the value of the surrounding regions for all the simulations performed in our study. These recharge values are identified as baseline recharge conditions in our study.

We model different recharge scenarios which present increased or decreased recharge values with respect to the baseline recharge conditions described above. We analyze the impact of recharge shifts on different decision (or performance) metrics: the temporal evolution of ^{3}H concentration at the same two observation wells of Bea et al. (2013), shown in Figure 2: (1) the source-zone UUTRA well (FSB95D) and (2) the downgradient UUTRA well (FSB110D). Both wells span the upper aquifer. Please note that we computed the contaminant concentration by taking the average value of the concentration reported at a set of observation points equally spaced within a given well in the upper aquifer. In addition, we evaluate the ^{3}H export at the CP to the Fourmile Branch Creek (see Figure 2), which is the main risk pathway at this site. The CP is defined at the seepage face (indicated in Figure 2) where the groundwater flow reaches the surface.

The concentrations are compared with the EPA's MCL for ^{3}H. Although the MCL criteria is not used for compliance purposes at the SRS, it has been used to evaluate the timeframe for the site closure and transfer (Denham and Eddy-Dilek, 2017).

3.2 Modeling scenarios

Previous studies on the SRS have reported an overall trend towards greater rainfall in the region (Faybishenko et al., 2018). According to the National Climate Assessment, South Carolina is expected to see precipitation increases of 10%-20% by 2100 (see Fig. 7.5 in Easterling et al. (2017)), as well as more extreme precipitation event by up to two-folds (see Fig 7.6 in Easterling et al. (2017)). Even if the amount of precipitation is not necessarily equal to the recharge, we assume that we can investigate the impact of climate change by simulating a range of different recharge values. The range would also account for the uncertainty associated with the climate projections. We mainly focus on increased natural recharge conditions, although, for completeness, we also investigate the impact of reduced recharge. Figure 3 provides an illustration of the recharge scenarios simulated in our analysis. We consider a baseline recharge, denoted as R_B, and indicated by the black line in Figure 3. To study the effect of climate change-induced increased/decreased recharge on contaminant transport, we define ϵ to be a perturbation from the baseline recharge and R_P to identify the perturbed recharge. We develop four perturbed recharge scenarios with respect to the baseline recharge conditions, corresponding to $\epsilon = 0$, described in the Section 3.1. The recharge perturbation starts at a certain time, set to year 2020, and is illustrated with a specific color for each scenario in Figure 3. In the following, we provide a detailed description of the scenarios and of the values adopted for ϵ and we employ t^* to indicate year 2020.

Figure 3: Schematic illustration of the perturbed recharge scenarios analyzed in the study: (1) the constant positive recharge shift starting in 2020 (green line), (2) the constant negative recharge shift starting in 2020 (blue line), (3) the one-year extreme recharge in 2020 (magenta line) and (4) the hypothetical cap failure and constant positive recharge shift starting in 2020 (green line). The baseline recharge scenario is denoted by the horizontal black line.

Constant positive recharge shift The recharge conditions of the first scenario (portrayed in green, from year 2020, in Figure 3) are illustrated through the following equation:

$$R_P(t) = \begin{cases} R_B, & if\ t < t^* \\ R_B(1+\epsilon), & if\ t \geq t^* \end{cases} \quad (1)$$

through this scenario we simulate a constant positive shift (i.e., an increase) of recharge from 2020 until the end of the simulation, set to year 2100. The perturbation ϵ assumes the following range of values: ϵ = [0.1, 0.2, 0.3, 0.4, 0.5], we therefore simulate a recharge increase of +10% to +50% compared to baseline recharge conditions.

Constant negative recharge shift By the same token, the second scenario (blue line from year 2020 in Figure 3) is illustarted through the following equation:

$$R_P(t) = \begin{cases} R_B, & if\ t < t^* \\ R_B(1-\epsilon), & if\ t \geq t^* \end{cases} \quad (2)$$

this scenario is characterized by a constant negative shift of recharge (i.e., a decrease) of -10% to -50% (ϵ = [0.1, 0.2, 0.3, 0.4, 0.5] from equation (2)) within the timeframe 2020-2100.

One-year extreme recharge The third scenario (magenta line from 2020 in Figure 3) is described by:

$$R_P(t) = \begin{cases} R_B, & if\ t < t^* \\ R_B(1+\epsilon), & if\ t^* \leq t \leq t^* + 1 \end{cases} \quad (3)$$

this scenario considers a significant increase of recharge within year 2020, mimicking an extreme precipitation event of a factor of 1.5, 2, 5 and 10 folds compared to baseline conditions. The range of perturbation values of this third scenario, according to equation (3), are then: ϵ = [0.5, 1, 4, 9].

Cap failure and constant positive recharge shift The cap failure is also evaluated in conjunction with the natural recharge shift. Although low-permeability material is used for capping the F-Area basins, increased vegetation or other mechanisms could threaten the integrity of the source-zone capping structure (Worthy et al., 2013a, b, 2015). In the fourth scenario, we assume that the cap will fail at the same time of the recharge increase (i.e., in year 2020). Note that the assumption of cap failure in 2020 is solely for the purpose of the modeling exercise and not a prediction of actual cap failure. The perturbed recharge conditions of this scenario are then the same of the first

scenario, i.e.:

$$R_P(t) = \begin{cases} R_B, & if\ t < t^* \\ R_B(1+\epsilon), & if\ t \geq t^* \end{cases} \quad (4)$$

The cap failure is represented by increased source-zone recharge to the level of the surrounding region, therefore we hypothesize a complete failure of the containment structure. Although such a sudden failure is unlikely to happen, we assume instant failure to evaluate the most extreme case. The fourth scenario simulates the failure of the capping structure in arbitrarily assumed year 2020 under baseline recharge conditions and under the increased recharge conditions of the first scenario, characterized by ϵ = [0.1, 0.2, 0.3, 0.4, 0.5], from 2020 to 2100.

In reality, such precipitation/recharge changes are expected to occur gradually or randomly rather than through the step change assumed in this analysis. However, such simple representations would facilitate our fundamental understanding of various complex impacts of climatic changes on contaminant concentrations and exports.

For the conditions explored in this study (Figure 3) we expect that the changes in the recharge rates (as described in the scenarios above) will impact the concentration breakthrough curves (BTCs) by local dilution as well as by affecting the rate at which the contaminant mass is released from the vadose zone to the groundwater system. Figure 4 schematically pictures the contaminant BTC under baseline conditions and perturbed recharge conditions. We expect that, increased recharge (relative to the baseline values) causes a slight dilution (Phase I in Figure 4) followed by a "rebound" effect in the concentration BTC (Phase II in Figure 4) due to the mobilization of the solute mass located in proximity of the source (Figure 4).

Figure 4: Schematic illustration of the impact of increased recharge on the concentration breakthrough curve (BTC) at an observation well located downgradient from the source zone. The recharge rate increase causes a slight dilution (Phase I), followed by a "rebound" effect in the BTC (Phase II) due to contaminants' mobilization. The continuous blu curve indicates the BTC under baseline recharge whereas the dashed red curve corresponds to the concentration BTC under a change in the recharge conditions (see inset figure).

4 Results and Discussion

4.1 Spatiotemporal Dynamics of the Contaminant Plume

Prior to investigating the effects of recharge on transport observables at specific wells and at the CP, we provide snapshots of the simulated contaminant plume in the coupled vadose zone-groundwater system (Figure 5) for the baseline case. Figure 5 shows the plume migration at different years, namely 1961 (Figure 5b), 1988 (Figure 5c), 2000 (Figure 5d) and 2033 (Figure 5e).

Figure 5: Illustration of the simulated tritium plume in the SRS. The initial condition is displayed in panel (a). The plume snapshots are shown for years (b) 1961, (b) 1988, (c) 2000 and (d) 2033.

As observed in Bea et al. (2013), the contaminant plume first moves downward in the vadose zone, and then spreads laterally below the groundwater table (Figure 5b). During the operation, most of the plume migrates within the upper aquifer, although a part of the plume penetrates the TCCZ and reaches the lower aquifer (Figure 5c). After the operation ends, the clean water front arrives from upstream and pushes the plume downgradient (Figure 5d). The contaminant plume displays a stratified distribution since the residual contaminants in the vadose zone constitute a persistent contamination source and the low-permeability TCCZ becomes a secondary source. As displayed in Figure 5e, in year 2033 the vadose zone and TCCZ continue to be the residual contaminant sources.

4.2 Contaminant concentration and export BTCs

We first compare the temporal evolution of the ^3H concentrations [mol kgw $^{-1}$] at the observation wells and of the ^3H export [mol y $^{-1}$] at the CP among different recharge scenarios (Figures 6-9) for 0-100 years forward from the assumed recharge perturbations and cap failure (i.e., within the timeframe 2020-2100). Under baseline recharge conditions (indiated by $\epsilon = 0$ in Figures 6-9), ^3H concentrations and export generally decrease within the timeframe 2020-2100, given that the peak concentration and export occur closer to the contaminant discharge operation timeframe (1955-1988), i.e., before year 2020.

Figure 6: Temporal evolution of ^3H concentration at the: (a) source-zone well, (b) downgradient well and (c) ^3H export at the CP for the baseline scenario, indicated by $\epsilon = 0$, and the constant positive recharge shift scenario, characterized by $\epsilon = 0.1, 0.2, 0.3, 0.4, 0.5$. The results of different

recharge perturbations are portrayed in different colors. The thin horizontal dashed black line represents the MCL for ^3H.

Figure 7: Temporal evolution of ^3H concentration at the: (a) source-zone well, (b) downgradient well and (c) ^3H export at the CP for the baseline scenario, indicated by $\epsilon = 0$, and the constant negative recharge shift scenario, characterized by $\epsilon = 0.1, 0.2, 0.3, 0.4, 0.5$. The results of different recharge perturbations are portrayed in different colors. The thin horizontal dashed black line represents the MCL for ^3H.

Figure 8: Temporal evolution of ^3H concentration at the: (a) source-zone well, (b) downgradient well and (c) ^3H export at the CP for the baseline scenario, indicated by $\epsilon = 0$, and the one-year extreme recharge scenario, characterized by $\epsilon = 0.5, 1, 4, 9$. The results of different recharge perturbations are portrayed in different colors. The thin horizontal dashed black line represents the MCL for ^3H.

Figure 9: Temporal evolution of ^3H concentration at the: (a) source-zone well, (b) downgradient well and (c) ^3H export at the CP for the baseline scenario, indicated by $\epsilon = 0$, the cap failure under the baseline scenario, indicated by $\epsilon = 0^{(c)}$, and the cap failure under the constant positive recharge shift scenario, indicated by $\epsilon = 0.1^{(c)}, 0.2^{(c)}, 0.3^{(c)}, 0.4^{(c)}, 0.5^{(c)}$, with $^{(c)}$ indicating the capping failure. The results of different recharge perturbations are portrayed in different colors. The thin horizontal dashed black line represents the MCL for ^3H. The inset shows the log-scale plot.

When the positive constant shift of recharge occurs (Figure 6), the concentration initially decreases for approximately 2-10 years at the source-zone well (Figure 6a) and for around 5-20 years at the downgradient well (Figure 6b). This slight decrease of concentration is an outcome of dilution, attributed to the presence of more water in the system which enhances the mixing of the plume with clean water. We then observe a "rebound" in the concentrations due to the additional recharge, during which the concentration increases with respect to the concentration BTC obtained for the baseline case ($\epsilon = 0$). This is attributed to the fact that the residual contaminants in the

vadose zone are mobilized under higher recharge. As a consequence, more solute mass reaches the wells and the CP. The concentration increase during the "rebound" phase is more pronounced at the source-zone well (Figure 6a) than at the downgradient well (Figure 6b) given that the latter is located further away from the source zone and consequently less influenced by the mobilization of residual ^3H. These results are in agreement with previous theoretical analysis which showed that near-source locations are more sensitive to changes in the solute mass release at the source zone (de Barros, 2018). By comparing the effects of different magnitudes of recharge shifts on well concentrations, we notice that a recharge increase characterized by $\epsilon = 0.1$ does not influence the concentration BTC significantly. On the other hand, Figure 6a and 6b show that, for larger recharge, the timing of the "rebound" effect happens before and the corresponding peak concentration is higher (i.e., see concentration BTCs within the range $\epsilon = 0.2 - 0.5$). We also point out that the concentration decrease after the peak is generally more rapid as ϵ increases (see BTCs produced by $\epsilon = 0.4 - 0.5$ in Figure 6a-b). Indeed, under higher recharge, a bigger part of the residual ^3H is mobilized and flushed out of the aquifer system earlier in time. The export, on the other hand, slightly tends to increase but does not change significantly even under the maximum increase of recharge, indicated by $\epsilon = 0.5$ (Figure 6c). The minor effects on the export are attributed to the fact that the export is an integrated measure that incorporates the upwelling groundwater from the lower aquifer which is less affected by the recharge changes.

Decreased recharge (Figure 7) produces minor effects on well concentrations compared to increased recharge (compare Figure 6a-b to Figure 7a-b). Lower recharge causes a small increase in the concentration for around 5-20 years at the source-zone well (Figure 7a) and for approximately 10-20 years at the downgradient well (Figure 7b). Figure 7a depicts a higher peak concentration as ϵ increases. This effect takes place because a lower amount of water in the system decreases the dilution potential of the aquifer hence leading to an increase the concentration. The differences between the concentration BTCs obtained for different ϵ values at both observation wells in Figure 7a-b are less visible than in Figure 6a-b. We observe that increased recharge has a larger impact on the source-zone well (Figure 7a) than on the downgradient well (Figure 7b), whereas decreased recharge causes more uniform effects between the two observation wells. This is because the mobilization of ^3H caused by increased recharge has more impact closer to the source (Figure 7a), whereas the decrease of dilution, emerging from decreased recharge and resulting in higher concentration (Figure 7a-b) has a more uniform effect

on the aquifer system. Finally, minor effects are displayed on the export (Figure 7c), as noted also for increased recharge conditions (see Figure 6c). However we notice that the ^3H export tends to slightly decrease under negative recharge shifts given that less residual ^3H is mobilized from the vadose zone.

We next observe the outcomes of the third scenario (i.e., the one-year extreme recharge event) in Figure 8. One-year of extreme recharge significantly increases the well concentrations during the "rebound" phase over an extended period of time, i.e., for around 10-20 years (Figure 8a-b). We then observe that a short extreme event could affect the well concentrations for several decades. At the source-zone well (Figure 8a), prior to the "rebound" phase, the concentration decreases slightly after the perturbation event (in 2020) due to dilution, particularly under the most extreme scenario, indicated by $\epsilon = 9$. On the other hand, at the downgradient well (Figure 8b), the concentration decrease due to dilution is more pronounced given that the plume has traveled a longer distance. Five-to-ten years after the initial dilution, the concentration increases, during the "rebound" phase. The extreme one-year precipitation indicated by $\epsilon = 0.5$ does not significantly affect the concentrations, especially at the downgradient well, where even the recharge scenario characterized by $\epsilon = 1$ does not produce significant changes when compared to baseline conditions ($\epsilon = 0$). We also observe that higher recharge shifts produce higher peak concentrations in the "rebound" phase due to the mobilization of the solute mass at the source zone (Figure 8a-b) as well as higher initial dilution. The effect of recharge changes on the export (Figure 7c) is minor compared to the influence on the concentrations in the wells (Figure 8a-b), although we observe a peak of the export around 2020 when $\epsilon = 9$.

Figure 9 reports the results obtained for the scenario characterized by the failure of the capping structure under baseline conditions and constant positive recharge shifts starting in 2020. Figure 9 shows that the concentration increase at the wells is significantly larger than the increase observed for undamaged source-zone capping conditions. The concentration "rebound" happens after 5-8 years at the source-zone well (Figure 9a) and after 10-15 years at the downgradient wells (Figure 9b). The export at the CP also shows a visible increase after around 2035 (Figure 9c). This is due to the fact that, under higher recharge and no capping structure, the bulk of residual contaminants in the vadose zone migrate to the groundwater system. We notice that the increase of concentration/export happens earlier in time at the well closer to the contaminant source zone, later at the downgradient well and even further when considering the export at the CP, located at the

right boundary of the domain. Moreover, as the recharge value increases, from $\epsilon = 0.1$ to $\epsilon = 0.5$, the peak concentration/export, caused by the additional recharge, becomes higher and occurs earlier in time (see Figure 9). The inset log-scale plot of Figure 9a shows that the extreme concentration increase resulting from the cap failure is followed by a rapid decrease of the concentration, as the ^3H plume is flushed out of the system earlier when the capping structure fails, moving the contamination problem downgradient. This effect is amplified as ϵ increases. The same observations apply to the downgradient well and to the export (see inset log-scale plot of Figure 9b-c). We finally notice that the difference between the BTCs given by different ϵ values is more pronounced when we assume that the cap fails (Figure 9).

The results of an additional recharge scenario, characterized by a range of positive recharge shifts within a timeframe shorter than a year, is presented in the Supplementary Material. These outcomes confirm that our findings also apply to a smaller time scale of hydrological shift.

4.3 Impact of recharge perturbations on key Environmental Performance Metrics

We quantify the impact of climate change-driven recharge shifts on key EPMs (e.g, peak contaminant concentration, early and late arrival times, time of exceedance of MCL). Given that the recharge shifts considered in our study start from year 2020 (after the discharge operation at the SRS F-Area terminated, i.e. during a contaminant concentration/export descending/tailing phase), we do not consider the peak concentration but we analyze the maximum change on the concentration and export BTCs induced by the recharge perturbations. Moreover we investigate the effect of recharge shifts on the time of exceedance of the MCL for ^3H .

4.3.1 Maximum difference between baseline and perturbed BTCs

We identify the maximum normalized difference between the contaminant concentration or export BTC obtained under baseline and perturbed recharge conditions as:

$$\gamma_c = \frac{1}{C_b(t_{d_{max}})} \max_t |C_b(t) - C_p(t)| \times 100, \tag{5}$$

where $C_b(t)$ and $C_p(t)$ in (5) are the contaminant concentration [mol kgw^{-1}] or contaminant export [mol y^{-1}] of the baseline (subscript "b") and the perturbed (subscript "p") recharge

scenarios respectively, whereas $C_b(t_{d_{max}})$ is the baseline concentration or export taken at the time where the difference between baseline and perturbed BTCs is maximum. The metric γ_c (5) is plotted in Figure 10 as a function of the recharge perturbation ϵ, whose values are described in Section 3.2. Note that, from (5), $\gamma_c = 0$ for the baseline scenario, indicated by $\epsilon = 0$. We recall that only a limited range of recharge perturbations were simulated in our analysis, therefore the comments below are based on a linear interpolation between γ_c and the analyzed ϵ values.

When the recharge is positively shifted by a constant value (Figure 10a), the relative change in the well concentrations, quantified by γ_c (5), exhibit a non-linear or step-function response to the perturbation ϵ. As shown in Figure 10a, γ_c at the source-zone well drastically increases (from around 10% to almost 120%) when the recharge perturbation ϵ changes from 0.1 to 0.2, while γ_c at the downgradient well is highly impacted (it changes from approximately 20% to 100%) when ϵ goes from 0.3 to 0.4. The changes are smaller during the other recharge shifts' intervals. Our results suggest the presence of a threshold, or trigger level of recharge, above which the well concentrations are significantly affected. This trigger level is lower at the source-zone well than at the downgradient well; a recharge corresponding to $\epsilon = 0.1$ could represent this threshold at wells closer to the source-zone, while a higher trigger level of recharge, approximately identified by $\epsilon = 0.3$, is identified downgradient. The export, on the other hand, increases in a quasi-linear manner with the recharge perturbation (Figure 10a). As shown in the concentration time series (see Figure 6c), the effect of recharge shifts on the export is significantly smaller compared to that on the well concentrations. Indeed a recharge shift corresponding to $\epsilon = 0.5$ results in a value of γ_c of approximately 20% when observing the CP export, while a recharge shift given by $\epsilon = 0.5$ produces values of γ_c of approximately 80%-100% at the observation wells.

Figure 10: Maximum difference between contaminant concentrations and export BTCs of the baseline scenario and the perturbed recharge scenarios (γ_c) versus perturbation (ϵ) for the constant positive recharge shift scenario (a), the constant negative recharge shift scenario (b), the one-year extreme recharge scenario (c), the cap failure and constant positive recharge shift scenario (d), where the superscript $^{(c)}$ indicates the capping failure. Results at the source-zone

well are illustrated in red, at the downgradient well are pictured in blue and at the CP are indicated in green.

Figure 10b shows the γ_c - ϵ relationship for the negative recharge shift scenario. Decreasing the recharge rate generally has a smaller impact on γ_c with respect to increased recharge conditions (compare the values of γ_c in Figure 10a and 10b), according to the results in Figure 7. We identify non-linear responses and trigger levels of recharge perturbation at the downgradient well and at the CP. The trigger levels are very small at the downgradient well (e.g., less than $\epsilon = 0.1$) and higher for the export (i.e., $\epsilon = 0.2$). The maximum difference between the baseline case and the perturbed BTC (computed via equation (5)) is larger at the downgradient well than at the source-zone well (see Figure 10b). This is different than what was observed from the results of the positive shift scenario. When comparing Figures 10a and 10b we observe that, under positive shifts of recharge (Figure 10a), γ_c evaluated at the source-zone is more sensitive to smaller ϵ values. In other terms, we could say that the source-zone well responds first to the perturbation ϵ. This is because the source-zone well is more impacted by the mobilization of ^3H given its proximity to the source. However, when the recharge decreases (Figure 10b), changes in γ_c are more prominent at the downgradient well for smaller perturbations ϵ, i.e., the downgradient well responds first than the source-zone well. Indeed, the changes in the concentration are more uniform between the source-zone well and the downgradient well (compare Figures 7a and 7b) under lower recharge because they happen due to the concentration (or less dilution) as opposed to the mobilization of contaminants. Moreover, these changes take place at a later time downgradient, when the baseline concentration is smaller, resulting in higher γ_c downgradient.

Under the extreme one-year recharge scenario (Figure 10c), the trigger-level is larger (around $\epsilon = 1$) when compared to the results obtained for the constant positive recharge shift scenario at both observation wells (compare Figures 10a and 10c). We observe that the γ_c-ϵ relationship is quite similar for the two observation wells until $\epsilon = 4$. However, when $\epsilon = 9$, the recharge increase impact at the downgradient well becomes quite significant. In quantitative terms, this impact is approximately two times that at the source zone well (compare red and blue lines in Figure 10c). Finally, the impact of the extreme event on the contaminant export is quite

limited and increases linearly with the perturbation ϵ (Figure 10c). However, a significant increase of the export is detected for the most extreme one-year precipitation event investigated in this study (i.e., when $\epsilon = 9$, γ_c equals 65%).

The cap failure scenario (Figure 10d) also shows a non-linear response when evaluating the sensitivities of the wells' concentrations and the export to the perturbation ϵ. We observe an extreme increase of γ_c caused by the signification mobilization of the residual contaminants entrapped in the vadose zone when the capping structure fails, confirming the importance of the latter containment system. Successive increases of recharge do not significantly affect the value of γ_c, i.e., γ_c reaches a plateau under capping failure conditions. The almost constant value of γ_c is generally higher at the source-zone well than at the donwgradient well and at the CP. Our analysis then suggests that the failure of the capping can be identified as a trigger situation after which major changes in both well concentrations and on the export are expected.

4.3.2 Difference of time above MCL between baseline and perturbed BTCs

In this Section, we identify the metric γ_t as the normalized difference of the time of exceedance of the MCL for ^3H between the baseline recharge scenario and the perturbed recharge scenarios as:

$$\gamma_t = \frac{1}{t(C_b(t) > MCL)} \left| t(C_b(t) > MCL) - t(C_p(t) > MCL) \right| \times 100. \quad (6)$$

with $t(C_b(t) > MCL)$ and $t(C_p(t) > MCL)$ respectively being the time [d] during which the contaminant concentration exceeds the EPA's MCL for ^3H for the baseline (subscript "b") and the perturbed (subscript "p") recharge scenarios. As before, the metric γ_t (6), expressed in percentage, is plotted as a function of ϵ for each recharge scenario in Figure 11 and, from (6), $\gamma_t = 0$ for the baseline scenario (i.e., when $\epsilon = 0$). Similarly to before, our observations are based on a linear interpolation between γ_t and the range of ϵ values considered.

Figure 11: Difference of time of exceedance of the MCL for ^3H between the baseline scenario and the perturbed recharge scenarios (γ_t) versus perturbation (ϵ) for the constant positive recharge shift scenario (a), the constant negative recharge shift scenario (b), the one-year extreme

recharge scenario (c), the cap failure and constant positive recharge shift scenario (d), where the superscript $^{(c)}$ indicates the capping failure. Results at the source-zone well are illustrated in red and results at the downgradient well are pictured in blue.

Under the positive shift of recharge scenario (Figure 11a), γ_t shows a non-linear response to the recharge perturbation ϵ at the source-zone well (in red). In this case, γ_t increases until its maximum value under a perturbation $\epsilon = 0.2$ and $\epsilon = 0.3$ but decreases afterwards. We then notice that the intermediate values of ϵ produce the highest influence on the timeframe of MCL exceedance, as compared to the highest values of ϵ. Indeed, positive recharge shifts initially dilute the plume in the tailing phase, and increase the ^3H mobilization, leading to an increase of the concentration during the "rebound" phase, but afterwards flush the plume out of the system, i.e., at a later stage the ^3H concentration values reach the ^3H MCL faster (see BTCs characterized by $\epsilon = 0.4 - 0.5$ in Figure 6a). The higher the recharge, the higher is the concentration "rebound" peak and the faster the plume is flushed out of the aquifer, therefore the maximum increase of the time above MCL is produced by intermediate value of recharge (for example given by $\epsilon = 0.2, 0.3$). On the other hand, γ_t (6) increases almost linearly with the permanent positive recharge perturbation at the downgradient well (in blue) but the maximum change of γ_t (6) with respect to the baseline recharge scenario is only around 15%.

Decreased recharge (Figure 11b) also results in a non-linear response of γ_t to ϵ. Compared to the positive recharge shift scenario in which the source-zone well responds first (Figure 11a), when the recharge is negatively shifted (Figure 11b), the downgradient well responds first. A decrease of the natural recharge does not significantly influence the time when the ^3H concentration exceeds MCL at the source-zone well (in red) given that the minor concentration increase takes place when the baseline concentration exceeds the MCL. However we identify the value of $\epsilon = 0.2$ as the trigger level of recharge decrease after which the time above MCL is significantly affected at the downgradient well (in blue). The remaining recharge steps produce less significant changes at the downgradient well.

One-year of extreme recharge produces relatively smaller changes in the time above MCL as compared to the effect of permanent shifts of recharge when $\epsilon < 1$ (compare Figure 11c with Figure 11a). This scenario does not influence much the time of MCL exceedance at the

source-zone well (in red), where a maximum γ_t around 20% is identified when $\epsilon = 4$. Nevertheless, the response at the downgradient well, also non-linear, shows a trigger level represented by $\epsilon = 1$ above which the time of exceedance of MCL is highly impacted. This significant impact takes place because the increase of concentration downgradient, which results in values above the ^3H MCL, happens later in time, compared to the upgradient well, when the baseline concentration is already below the MCL.

When the capping structure fails (Figure 11d), we notice that γ_t reaches the maximum value at both wells, similarly to what observed when looking at the γ_c - ϵ results. The value of γ_t then decreases at both wells when the recharge increases in the presence of no cap. This decrease is almost linear at the source-zone well. In the overall, we observe that the capping failure is identified as a trigger condition which causes an important increase of both EPMs (as quantified by γ_c and γ_t), therefore a substantial risk increase.

When comparing the results in Figures 10 and 11 we understand that different recharge's thresholds/trigger levels are identified depending on the metric of interest for environmental remediation (for instance the maximum concentration/export BTC's change or the time of exceedance of MCL's change caused by the recharge perturbations), the location of the observation location and the measured variable (e.g., contaminant concentration or contaminant export).

5 Summary and Conclusions

In this paper we investigate the impact of climate change-driven aquifer's recharge shifts on residual contaminants in soil and groundwater subject to sustainable remediation. For the sake of simplicity we assume that the changes in precipitation and temperature can be translated into changes of the natural aquifer's recharge. We establish the evaluation methodology, including the development of potential future scenarios on the basis of national climate assessments, site-specific model developments, and evaluation criteria. We illustrate four scenarios characterized by a range of variable recharge values: (1) constant positive recharge shift after a certain year (2) constant negative recharge shift after a certain year, (3) one-year of extreme recharge, (4) cap failure and constant positive recharge shift. Our methodology is demonstrated by

simulating the ^3H plume migration within the US DOE's nuclear reservation Savannah River Site F-Area. We employ the unsaturated-saturated flow model Amanzi, calibrated and verified using site data.

In summary, our results generally show that changes of the recharge regime (even small) can significantly affect contaminant concentrations. The most noticeable outcome is the concentration "rebound" effect taking place, after an initial slight dilution, under higher recharge and/or capping failure conditions, which is given by the mobilization of the contaminant mass from the source zone and its transfer to the aquifer system. The concentration "rebound" effect is more pronounced and happens earlier as the recharge perturbation increases. Decreased recharge conditions could also cause a small concentration increase attributed to a decrease in the dilution potential of the aquifer. On the other hand, the ^3H export at the CP is only minimally influenced by recharge shifts, except for some extreme recharge scenarios. Trigger levels of recharge which highly impact the concentration BTC at the wells are identified. These threshold/trigger levels depend on the observation location and on the EPM under investigation, quantified through γ_c and γ_t. The latter display a non-linear response to the perturbation ϵ. For example, it is interesting to observe that the most significant influence on the time of exceedance of MCL under positive recharge shifts (i.e., first scenario) is identified under recharge values in the middle of the range considered given that higher ϵ values cause a steeper decrease of the concentration after the "rebound" phase, i.e., the concentration reaches the MCL faster.

Our results suggest that close monitoring of wells concentrations should be adopted during precipitation (connected to higher aquifers' recharge) and drought (connected to lower aquifers' recharge) periods, however the actual risk of the downgradient population, as quantified through the export, could be under control even when the well concentrations are remarkably impacted. Our findings constitute then immediate contribution to guide groundwater monitoring in the presence of increased climatic variabilities, particularly in explaining concentration anomalies. For example, without a proper understanding, the concentration increase, due to higher or lower recharge, could be mistaken, for instance attributed to additional leaks or contaminant sources. In addition, our analysis indicates that source-zone wells are critical to early detect mobilized residual contaminants under increased recharge or cap failure conditions. It would be advantageous to have more frequent sampling or in situ monitoring in the proximity of the contaminant source zones as an early warning system (Schmidt et al., 2018). Aside from

monitoring the contaminant concentration, characterizing the hydraulic fluxes in the vicinity of the source zone can also aid in understanding the macro-dispersive behavior of the plume and corresponding risks to the environment and public health (de Barros and Nowak, 2010; Henri et al., 2016). Our work also emphasizes the importance of properly maintaining the capping structure not only to sequester residual contaminants but also to reduce the uncertainty associated with climate variability, in fact the difference among recharge scenarios is smaller when the cap is undamaged.

We finally highlight that currently, simplified models adopting conservative assumptions are often used for performance and risk assessments at contaminated sites. Conservative approaches usually assume the worst case scenario, associated with higher recharge rates or higher permeability values to increase the plume mobility. The modeling scenarios investigated in this work, however, call into question the appropriateness of such conservative approaches, in fact the non-trivial trade-offs arising from the interplay between dilution and contaminants' mobilization require the use of more realistic and accurate flow and transport simulations, achieved through proper calibration processes, as well as probabilistic risk assessments (Maxwell et al., 2008; de Barros and Rubin, 2008; Siirila and Maxwell, 2012; Atchley et al., 2013; Libera et al., 2017). Overall, the trade-offs identified in our work must be evaluated with respect to the specific time, location and performance metric under investigation. Understanding these trade-offs would enable better allocation of available resources towards reducing uncertainty in decision making (de Barros et al., 2009, 2012).

Our work could be expanded by considering a more complex geochemistry setting, as well as surface water processes (e.g., evapotranspiration), and land model components (e.g., vegetation) of the SRS F-Area. Additionally, this study would benefit from an inclusion of different conceptualization of the aquifer's heterogeneous properties together with remediation strategies located at the site (e.g., pump and treat, funnel and gate systems). In particular, the effect of geological heterogeneity should be explored in more detail given that it can significantly augment contaminant plume mixing rates (de Barros et al., 2015).

Acknowledgements

This material is based upon work supported as part of the ASCEM project, which is funded by the

U.S. Department of Energy, Office of Environmental Management, and as part of the Lawrence Berkeley National Laboratory Science Focus Area, which is funded by the U.S. Department of Energy, Office of Science, Office of Biological and Environmental Research, both under Award Number DE-AC02-05CH11231 to Lawrence Berkeley National Laboratory. This research used resources of the National Energy Research Scientific Computing Center, a DOE Office of Science User Facility supported by the Office of Science of the U.S. Department of Energy under Contract No. DE-AC02-05CH11231. We thank Christiana Patricola for her valuable advice on climate data and assumptions. The first and second authors acknowledge the support by the National Science Foundation under Grant No. 1654009. Finally, we thank two anonymous reviewers for the constructive comments.

References

Atchley, A. L., Maxwell, R. M., and Navarre-Sitchler, A. K. (2013). Human health risk assessment of CO2 leakage into overlying aquifers using a stochastic, geochemical reactive transport approach. *Environ. Sci. Technol.*, 47(11):5954–5962.

Bea, S. A., Wainwright, H., Spycher, N., Faybishenko, B., Hubbard, S. S., and Denham, M. E. (2013). Identifying key controls on the behavior of an acidic-U (VI) plume in the Savannah River Site using reactive transport modeling. *J. Contam. Hydrol.*, 151:34–54.

Bloomfield, J. P., Williams, R. J., Gooddy, D. C., Cape, J. N., and Guha, P. (2006). Impacts of climate change on the fate and behaviour of pesticides in surface and groundwater-a UK perspective. *Sci. Total Environ.*, 369(1-3):163–177.

da Veiga, L. B., Lipnikov, K., and Manzini, G. (2014). *The mimetic finite difference method for elliptic problems*, volume 11. Springer.

Dai, M., Kelley, J. M., and Buesseler, K. O. (2002). Sources and migration of plutonium in groundwater at the Savannah River Site. *Environ. Sci. Technol.*, 36(17):3690–3699.

Darracq, A., Greffe, F., Hannerz, F., Destouni, G., and Cvetkovic, V. (2005). Nutrient transport scenarios in a changing Stockholm and Malaren valley region, Sweden. *Water Sci. Technol.*, 51(3-4):31–38.

de Barros, F. P. J. (2018). Evaluating the combined effects of source zone mass release rates and aquifer heterogeneity on solute discharge uncertainty. *Adv. Water Resour.*, 117:140–150.

de Barros, F. P. J., Ezzedine, S., and Rubin, Y. (2012). Impact of hydrogeological data on measures of uncertainty, site characterization and environmental performance metrics. *Adv. Water Resour.*, 36:51–63.

de Barros, F. P. J., Fiori, A., Boso, F., and Bellin, A. (2015). A theoretical framework for modeling dilution enhancement of non-reactive solutes in heterogeneous porous media. *J. Contam. Hydrol.*, 175-176:72–83.

de Barros, F. P. J. and Nowak, W. (2010). On the link between contaminant source release conditions and plume prediction uncertainty. *Journal of contaminant hydrology*, 116(1-4):24–34.

de Barros, F. P. J. and Rubin, Y. (2008). A risk-driven approach for subsurface site characterization. *Water Resour. Res.*, 44(1):1–14.

de Barros, F. P. J., Rubin, Y., and Maxwell, R. M. (2009). The concept of comparative information yield curves and its application to risk-based site characterization. *Water Resour. Res.*, 45(6):1–16.

Denham, M. and Eddy-Dilek, C. (2017). Influences on effective decay rates of radionuclides in groundwater: F-Area Seepage Basins, Savannah River Site. *WM2017 Conf. Phoenix, Arizona, USA*.

Destouni, G. and Darracq, A. (2009). Nutrient cycling and N2O emissions in a changing climate: the subsurface water system role. *Environ. Res. Lett.*, 4(035008):1–7.

Easterling, D. R., Kunkel, K., Arnold, J., Knutson, T., LeGrande, A., Leung, L. R., Vose, R., Waliser, D., and Wehner, M. (2017). Precipitation change in the United States (https://science2017.globalchange.gov/chapter/front-matter-about/).

Ellis, D. E. and Hadley, P. W. (2009). Sustainable remediation white paper-Integrating sustainable principles, practices, and metrics into remediation projects. *Remediat. J.*, 19(3):5–114.

Famiglietti, J. S. (2014). The global groundwater crisis. *Nat. Clim. Chang.*, 4(11):945–948.

Faybishenko, B., Wainwright, H., Denham, M., Amidon, M., Millings, M., Flach, G., and Eddy-Dilek, C. (2018). Basic climatic and hydrological data mining and analytics of the Savannah River site F-Area, Report LBNL-2001173, Lawrence Berkeley National Laboratory, Berkeley, Calif., July 2018.

Flach, G. (2004). Groundwater flow model of the general separations area using Porflow (U). WSRC-TR-2004-00106.Westinghouse Savannah River Company LLC, Savannah River

Site, Aiken, SC 29808.

Flach, G. P., Crisman, S. a., and Molz, F. J. (2004). Comparison of single-domain and dual-domain subsurface transport models. *Ground Water*, 42(6-7):815–828.

Freshley, M., Hubbard, S. S., Flach, G., Freedman, V., Agarwal, D., Andre, B., Bott, Y., Chen, X., Davis, J., Faybishenko, B., Gorton, I., Murray, C., Moulton, D., Meyer, J., Rockhold, M., Shoshani, A., Steefel, C., Wainwright, H., and Waichler, S. (2012). Phase II Demonstration ASCEM United States Department of Energy.

Futter, M. N., Helliwell, R. C., Hutchins, M., and Aherne, J. (2009). Modelling the effects of changing climate and nitrogen deposition on nitrate dynamics in a Scottish mountain catchment. *Hydrol. Res.*, 40(2-3):153.

Gellens, D. and Roulin, E. (1998). Streamflow response of Belgian catchments to IPCC climate change scenarios. *J. Hydrol.*, 210(1-4):242–258.

Green, T. R., Taniguchi, M., Kooi, H., Gurdak, J. J., Allen, D. M., Hiscock, K. M., Treidel, H., and Aureli, A. (2011). Beneath the surface of global change: Impacts of climate change on groundwater. *J. Hydrol.*, 405(3-4):532–560.

Henri, C. V., Fernàndez-Garcia, D., and de Barros, F. P. (2016). Assessing the joint impact of DNAPL source-zone behavior and degradation products on the probabilistic characterization of human health risk. *Adv. Water Resour.*, 88(May):124–138.

Killian, T. H., Kolb, N. L., Corbo, P., and Marine, I. W. (1986). Environmental information document, F-Area seepage basins. Report No. DPST 85-704.E.I. du Pont de Nemours & Co, Savannah River Laboratory, Aiken SC 29808.

Li, R. and Merchant, J. W. (2013). Modeling vulnerability of groundwater to pollution under future scenarios of climate change and biofuels-related land use change: A case study in North Dakota, USA. *Sci. Total Environ.*, 447:32–45.

Libera, A., de Barros, F. P., and Guadagnini, A. (2017). Influence of pumping operational schedule on solute concentrations at a well in randomly heterogeneous aquifers. *J. Hydrol.*, 546:490–502.

Lipnikov, K., Svyatskiy, D., and Vassilevski, Y. (2010). A monotone finite volume method for advection-diffusion equations on unstructured polygonal meshes. *J. Comput. Phys.*, 229(11):4017–4032.

Maxwell, R. M., Carle, S. F., and Tompson, A. F. B. (2008). Contamination, risk, and

heterogeneity: On the effectiveness of aquifer remediation. *Environ. Geol.*, 54(8):1771–1786.

Maxwell, R. M. and Kastenberg, W. E. (1999). Stochastic environmental risk analysis: an integrated methodology for predicting cancer risk from contaminated groundwater. *Stoch. Environ. Res. Risk Assess.*, 13(1-2):27–47.

Middelkoop, H., Daamen, K., Gellens, D., Grabs, W., Kwadijk, J. C. J., Lang, H., Parmet, B. W. A. H., Schadler, B., Schulla, J., and Wilke, K. (2001). Impact of climate change on hydrological regimes and water resources management in the Rhine basin. *Clim. Change*, 49(1-2):105–128.

Mualem, Y. (1976). A new model for predicting the hydraulic conductivity of unsaturated porous media. *Water resources research*, 12(3):513–522.

O'Connell, S. and Hou, D. (2015a). Resilience: a new consideration for environmental remediation in an era of climate change. *Remediat. J.*, 26(1):57–67.

O'Connell, S. and Hou, D. (2015b). Surfactant-oxidation co-application for soil and groundwater remediation. *Remediat. J.*, 26(1):57–67.

Olesen, J. E., Carter, T. R., Díaz-Ambrona, C. H., Fronzek, S., Heidmann, T., Hickler, T., Holt, T., Minguez, M. I., Morales, P., Palutikof, J. P., Quemada, M., Ruiz-Ramos, M., Rubæk, G. H., Sau, F., Smith, B., and Sykes, M. T. (2007). Uncertainties in projected impacts of climate change on European agriculture and terrestrial ecosystems based on scenarios from regional climate models. *Clim. Change*, 81(SUPPL. 1):123–143.

Park, M. J., Park, J. Y., Shin, H. J., Lee, M. S., Park, G. A., Jung, I. K., and Kim, S. J. (2010). Projection of future climate change impacts on nonpoint source pollution loads for a forest dominant dam watershed by reflecting future vegetation canopy in a soil and water assessment tool model. *Water Sci. Technol.*, 61(8):1975–1986.

Pfister, L., Kwadijk, J., Musy, A., Bronstert, A., and Hoffmann, L. (2004). Climate change, land use change and runoff prediction in the rhine–meuse basins. *River Res. Appl.*, 20(3):229–241.

Phifer, M., Millings, M., and Flach, G. (2006). Hydraulic property data package for the e-area and z-area soils. *Cementitious Materials and Waste Zones, Washington Savannah River Company, Savannah River Site, Aiken, South Carolina*.

Sassen, D. S., Hubbard, S. S., Bea, S. A., Chen, J., Spycher, N., and Denham, M. E. (2012).

Reactive facies: An approach for parameterizing field-scale reactive transport models using geophysical methods. *Water Resour. Res.*, 48(10):1–20.

Schiedek, D., Sundelin, B., Readman, J. W., and Macdonald, R. W. (2007). Interactions between climate change and contaminants. *Mar. Pollut. Bull.*, 54(12):1845–1856.

Schmidt, F., Wainwright, H. M., Faybishenko, B., Denham, M., and Eddy-Dilek, C. (2018). In situ monitoring of groundwater contamination using the kalman filter. *Environ. Sci. Technol.*, 52(13):7418–7425.

Siirila, E. R. and Maxwell, R. M. (2012). A new perspective on human health risk assessment: Development of a time dependent methodology and the effect of varying exposure durations. *Sci. Total Environ.*, 431:221–232.

Sjoeng, A. M. S., Kaste, O., and Wright, R. F. (2009). Modelling future NO3 leaching from an upland headwater catchment in SW Norway using the MAGIC model: II. Simulation of future nitrate leaching given scenarios of climate change and nitrogen deposition. *Hydrol. Res.*, 40(2-3):217–233.

Tokunaga, T. K., Wan, J., and Denham, M. E. (2012). Estimates of vadose zone drainage from a capped seepage basin, F-Area, Savannah River Site. *Vadose Zone Journal*, 11(3).

US Environmental Protection Agency, https://www.epa.gov/brownfields.

US Environmental Protection Agency, https://www.epa.gov/superfund.

Van Bokhoven, A. (2006). The impact of climate change on the water quality of the Rhine river. *Kiwa Water Research (147 pp.)*.

Van Vliet, M. and Zwolsman, J. (2008). Impact of summer droughts on the water quality of the meuse river. *J. Hydrol.*, 353(1-2):1–17.

Visser, A., Kroes, J., Van Vliet, M. T. H., Blenkinsop, S., Fowler, H. J., and Broers, H. P. (2012). Climate change impacts on the leaching of a heavy metal contamination in a small lowland catchment. *J. Contam. Hydrol.*, 127(1-4):47–64.

Wainwright, H., Faybishenko, B., Molins, S., Davis, J., Arora, B., Pau G., Johnson, J., Flach, G., Denham, M., Eddy-dilek, C., Moulton, D., Lipnikov, K., Gable, C., Miller, T., and Freshley, M. (2016). Effective long-term monitoring strategies by integrating reactive transport models with in situ geochemical measurements 16212. *WM2016 Conf.*, pages 1–15.

Wainwright, H., Molins, S., Davis, J., Arora, B., Faybishenko, B., Krishnan, H., Hubbard, S., Flach, G., Denham, M., and Eddy-Dilek, C. (2015). Using ASCEM modeling and

visualization to inform stakeholders of contaminant plume evolution and remediation efficacy at F-Basin Savannah River, SC. *WM2015 Conf.*, pages 1–14.

Wainwright, H. M., Chen, J., Sassen, D. S., and Hubbard, S. S. (2014). Bayesian hierarchical approach and geophysical data sets for estimation of reactive facies over plume scales. *Water Resour. Res.*, 50(6):4564–4584.

Whitehead, P., Wilby, R., Battarbee, R., Kernan, M., and Wade, A. J. (2009). A review of the potential impacts of climate change on surface water quality. *Hydrological Sciences Journal*, 54(1):101–123.

Wilby, R. L., Whitehead, P. G., Wade, A. J., Butterfield, D., Davis, R. J., and Watts, G. (2006). Integrated modelling of climate change impacts on water resources and quality in a lowland catchment: River Kennet, UK. *J. Hydrol.*, 330(1-2):204–220.

Worthy, W., Abkowitz, M. D., and Clarke, J. H. (2015). A systematic approach to the evaluation of rcra disposal facilities under future climate-induced events. *Remediat. J.*, pages 71–81.

Worthy, W., Clarke, J. H., and Abkowitz, M. D. (2013a). Near-surface disposal performance assessment: Modeling monthly precipitation and temperature in various climate environments. *Remediat. J.*, pages 99–108.

Worthy, W., Clarke, J. H., and Abkowitz, M. D. (2013b). Surfactant-Oxidation Co-Application for soil and groundwater Remediation. *Remediat. J.*, 26(2):101–108.

Zachara, J. M., Long, P. E., Bargar, J., Davis, J. A., Fox, P., Fredrickson, J. K., Freshley, M. D., Konopka, A. E., Liu, C., McKinley, J. P., Rockhold, M. L., Williams, K. H., and Yabusaki, S. B. (2013). Persistence of uranium groundwater plumes: Contrasting mechanisms at two DOE sites in the groundwater-river interaction zone. *J. Contam. Hydrol.*, 147:45–72.

Supplementary material

As explained through the paper, given the intrinsic uncertainties of climate predictions, our study considers a wide range of natural recharge values. Even so, the smallest time scale of recharge shift considered is one year, in the third scenario. Therefore we decided to simulate flow and transport for a fifth scenario characterized by a smaller time scale of recharge variability, i.e., 3 months (one trimester). In this case, the perturbed recharge, indicated as R_P, is expressed as:

$$R_P(t) = \begin{cases} R_B, & if\ t < t^* \\ R_B(1+\epsilon)^n, & if\ t^* \le t \le t^* + 1 \end{cases} \quad (7)$$

In equation (7), ϵ always indicates the recharge perturbation and $t^* = 2020$, whereas n indicates the trimester number within year 2020, i.e., $n = 1$ for the first trimester of 2020, $n = 2$ for the second trimester of 2020, $n = 3$ for the third trimester of 2020 and $n = 4$ for the fourth trimester of 2020. Therefore the fifth scenario simulates a positive shift of recharge by a factor ϵ every three months within year 2020, starting in 2020 and ending in 2021, indeed the recharge is set back to baseline values starting in year 2021. The recharge shift by a factor ϵ in 2020 is applied with respect to the recharge value of the precedent trimester and it starts from baseline recharge in 2020. The perturbation ϵ assumes the following range of values: ϵ = [0.1, 0.2, 0.3, 0.4, 0.5].

Figure 12: Temporal evolution of ^3H concentration at the: (a) source-zone well, (b) downgradient well and (c) ^3H export at the CP for the baseline scenario, indicated by $\epsilon = 0$, and the positive three months recharge shift scenario, characterized by $\epsilon = 0.1, 0.2, 0.3, 0.4, 0.5$. The results of different recharge perturbations are portrayed in different colors. The thin horizontal dashed black line represents the MCL for ^3H.

The temporal evolution of the ^3H concentrations [mol kgw^{-1}] at the observation wells and of the ^3H export [mol y^{-1}] at the CP for the fifth scenario within the timeframe 2020-2100 is presented in Figure 12. Under positive three months recharge shifts (Figure 12), the concentration initially slightly decreases for approximately 2-8 years at the source-zone well (Figure 12a) and for around 8-10 years at the downgradient well (Figure 12b) because of dilution, similarly to what observed for the first scenario (i.e., under a constant positive recharge shift). Also in this case we identify a concentration "rebound" phase afterwards, during which the concentration increases at both wells (Figure 12a-b). At the source-zone well, under the recharge shifts indicated by $\epsilon = 0.3 - 0.5$ we notice a subsequent decrease of concentration followed by a concentration "rebound" and so forth, caused by the different recharge increases during year 2020. We also observe that, as the perturbation ϵ is higher, the initial concentration decrease is generally shorter and more pronounced and the subsequent concentration peak is higher (Figure 12a-b), however

when $\epsilon = 0.1 - 0.2$ only minor effects with respect to the baseline concentration are identified, especially at the downgradient well.

When comparing Figure 12a and Figure 12b we observe that the BTC's pattern (i.e., slight initial decrease followed by a concentration rebound) is less pronounced and happens later in time in Figure 12b according to the fact that the downgradient well is further away from the source. In line with the outcomes of the other recharge scenarios, the recharge perturbation only causes minor changes of the contaminant export to the creek (Figure 12c).

The results of the fifth scenario confirm that the key findings of our study hold even when the recharge shifts are more frequent in time, which could represent a more realistic situation. In fact, we generally observe that, even when the time variability of the recharge shift is shorter (i.e., three months instead of a year or more years), the positive shift of recharge triggers a pattern in the concentration BTC characterized by a slight decrease followed by a concentration "rebound" phase. This confirms that, no matter what is the timescale of the recharge perturbation, increasing aquifers' natural recharge initially causes a slight decrease of the concentration followed by a concentration rebound effect. Indeed, the higher volume of water that enters the system initially results in dilution, and later produces an increase of the concentration attributed to the mobilization of residual ^3H under additional water.

Highlights

- Hydrological shifts affect contaminants through dilution and re-mobilization.
- Increased recharge causes dilution followed by significant concentration increase.
- Trigger recharge levels depend on observed metric and observation location.
- Adopt frequent wells concentrations' sampling during precipitation/drought periods.
- Capping is critical to sequester contaminants and reduce climatic uncertainty.

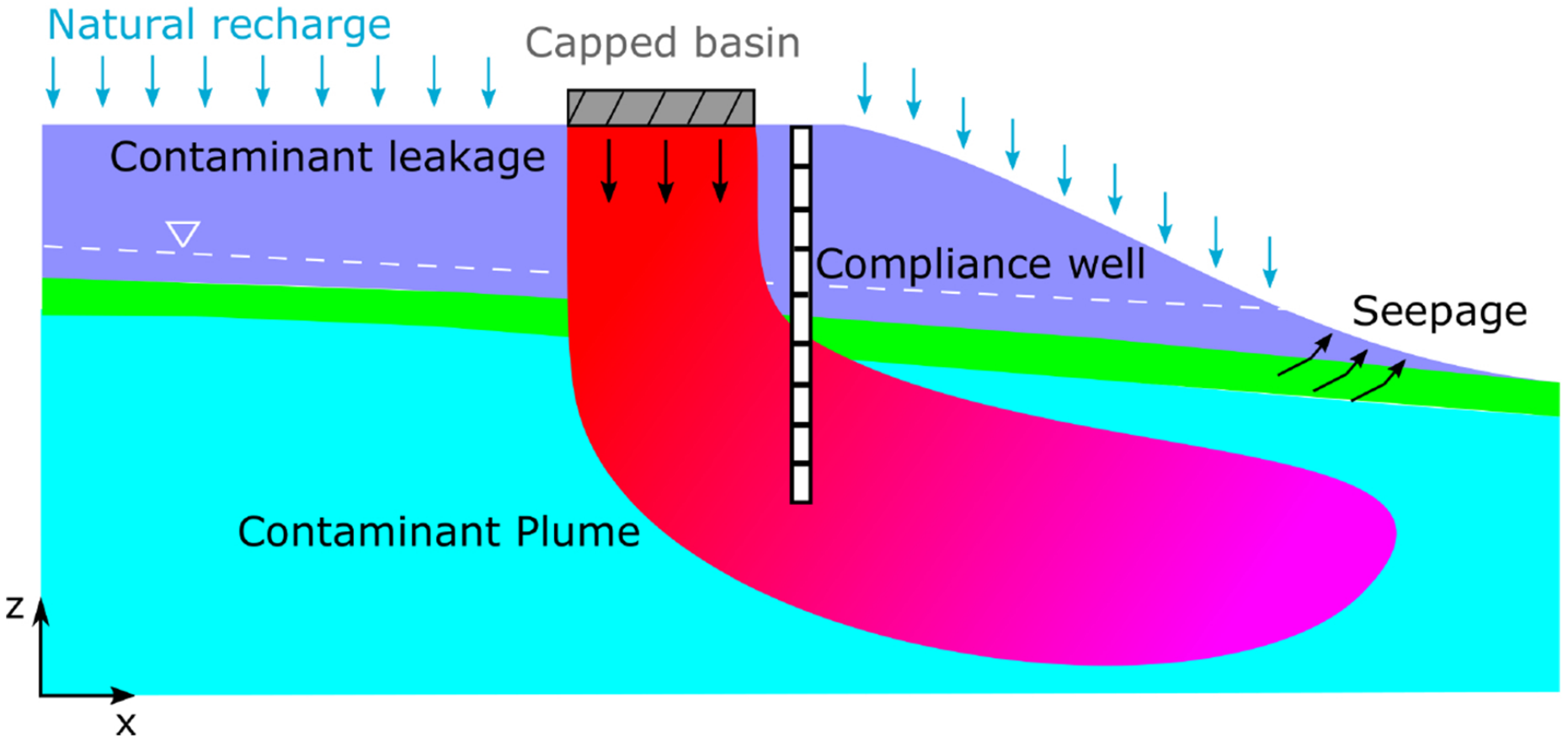
Natural recharge
Capped basin
Contaminant leakage
Compliance well
Seepage
Contaminant Plume
z
x

Figure 1

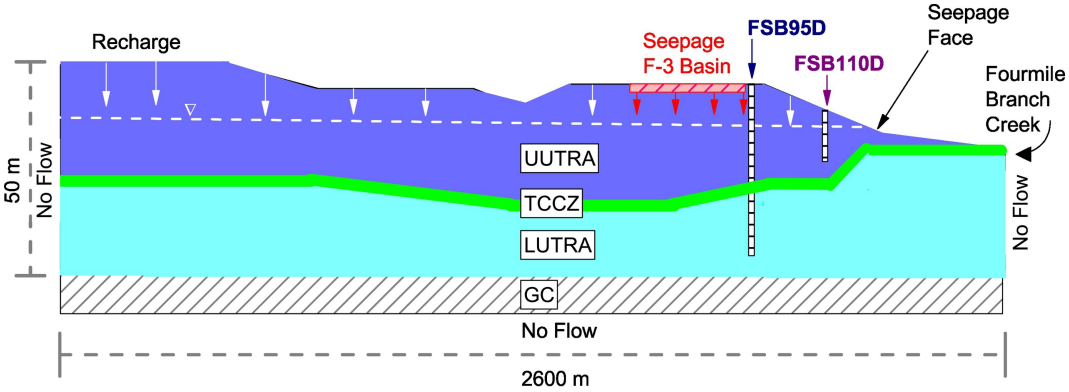

Hydrostratigraphic Units

UUTRA	Upper UTRA a.z
TCCZ	Tan Clay c.z.
LUTRA	Lower UTRA a.z
GC	Gordon c.z.

Figure 2

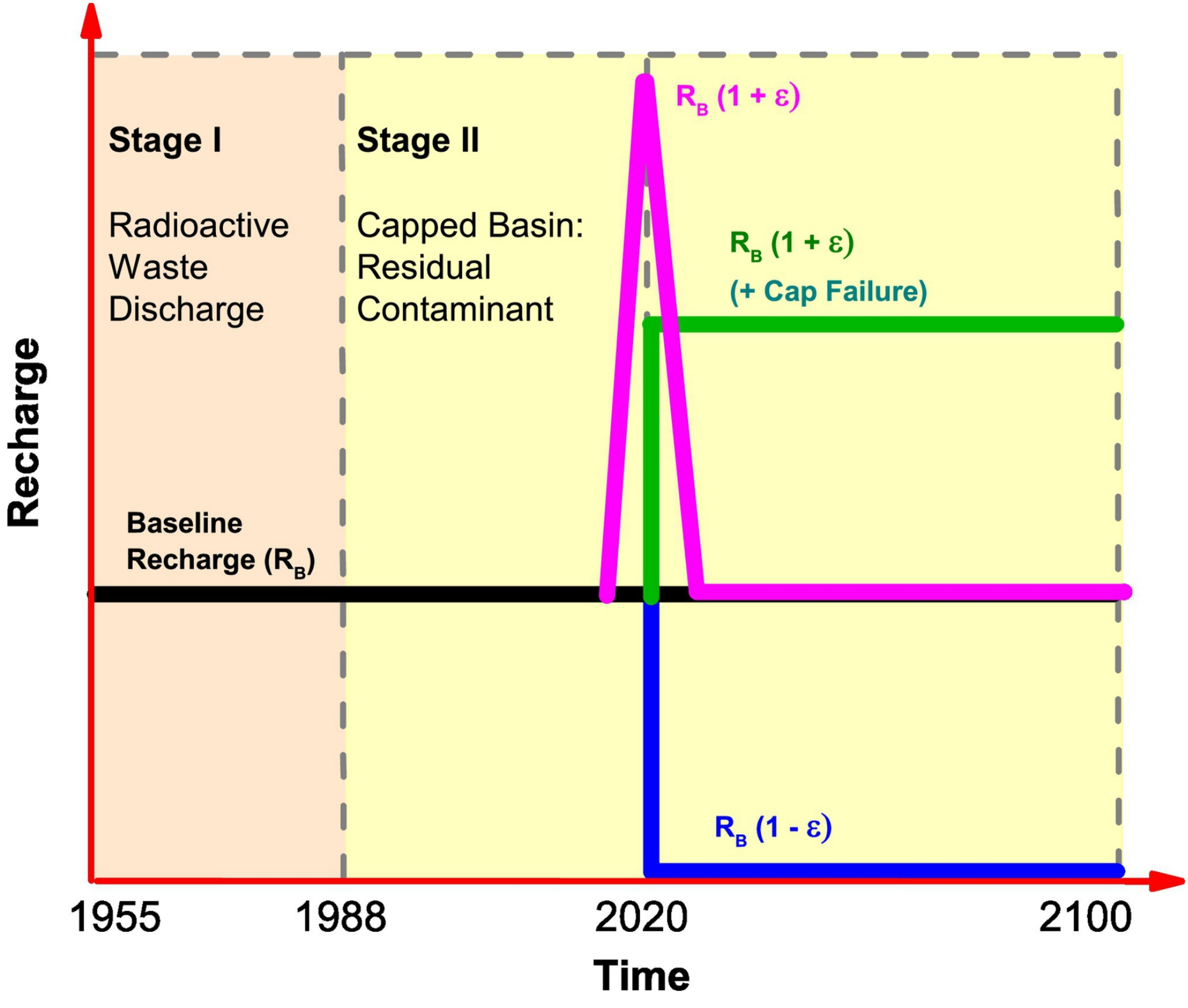
Stage I
Radioactive Waste Discharge
Stage II
Capped Basin: Residual Contaminant
R_B (1 + ε)
R_B (1 + ε)
(+ Cap Failure)
Baseline Recharge (R_B)
R_B (1 - ε)
Recharge
1955
1988
2020
2100
Time

Figure 3

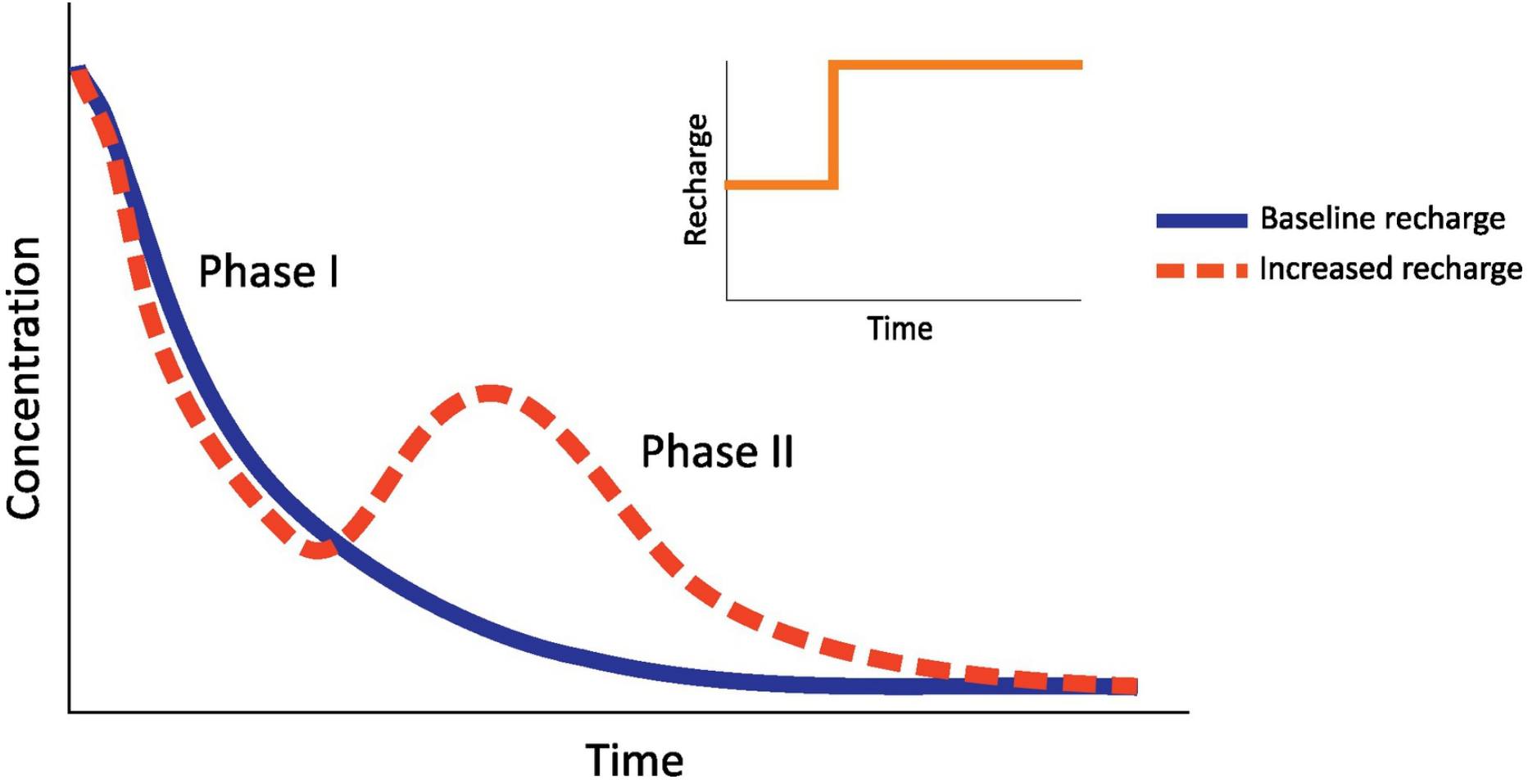
Concentration
Phase I
Phase II
Time
Recharge
Time
Baseline recharge
Increased recharge

Figure 4

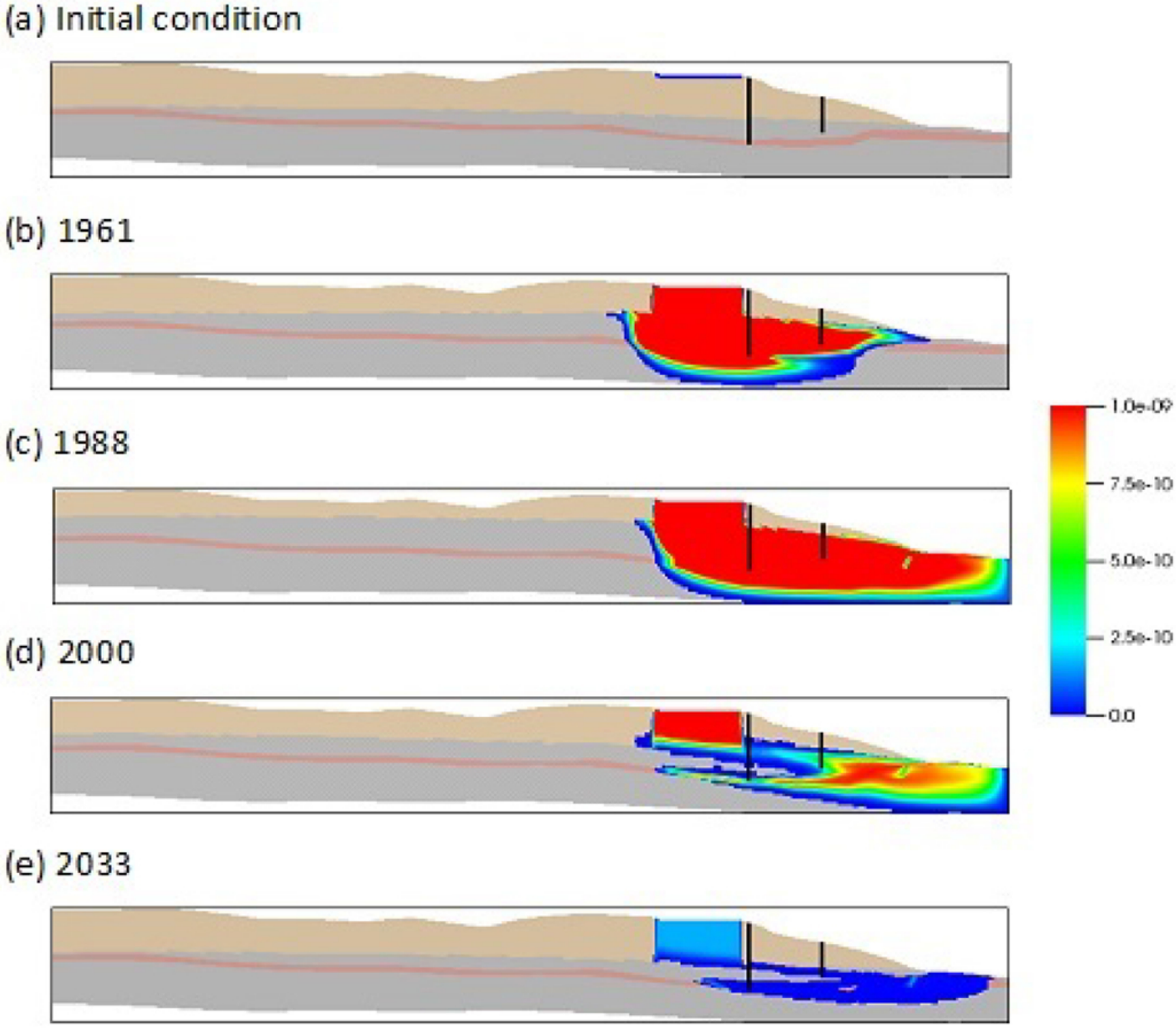
(a) Initial condition
(b) 1961
(c) 1988
(d) 2000
(e) 2033
1.0e-09
7.5e-10
5.0e-10
2.5e-10
0.0

Figure 5

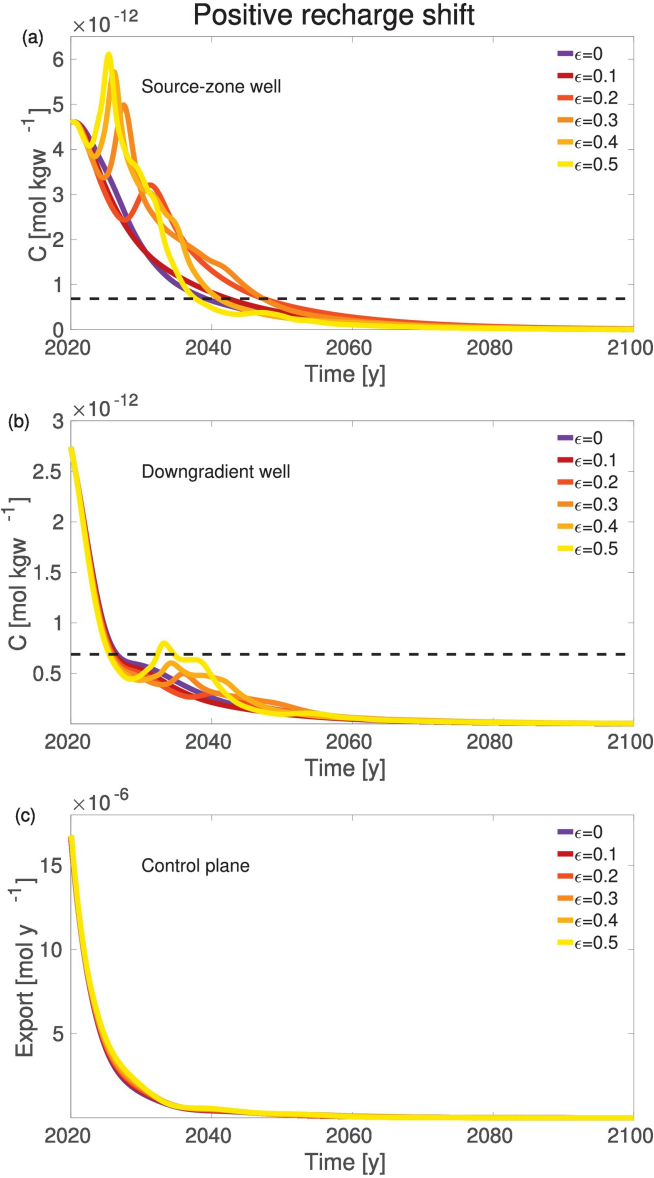
Positive recharge shift
(a)
×10^-12
Source-zone well
C [mol kgw^-1]
Time [y]
(b)
×10^-12
Downgradient well
C [mol kgw^-1]
Time [y]
(c)
×10^-6
Control plane
Export [mol y^-1]
Time [y]
ϵ=0
ϵ=0.1
ϵ=0.2
ϵ=0.3
ϵ=0.4
ϵ=0.5
2020
2040
2060
2080
2100

Figure 6

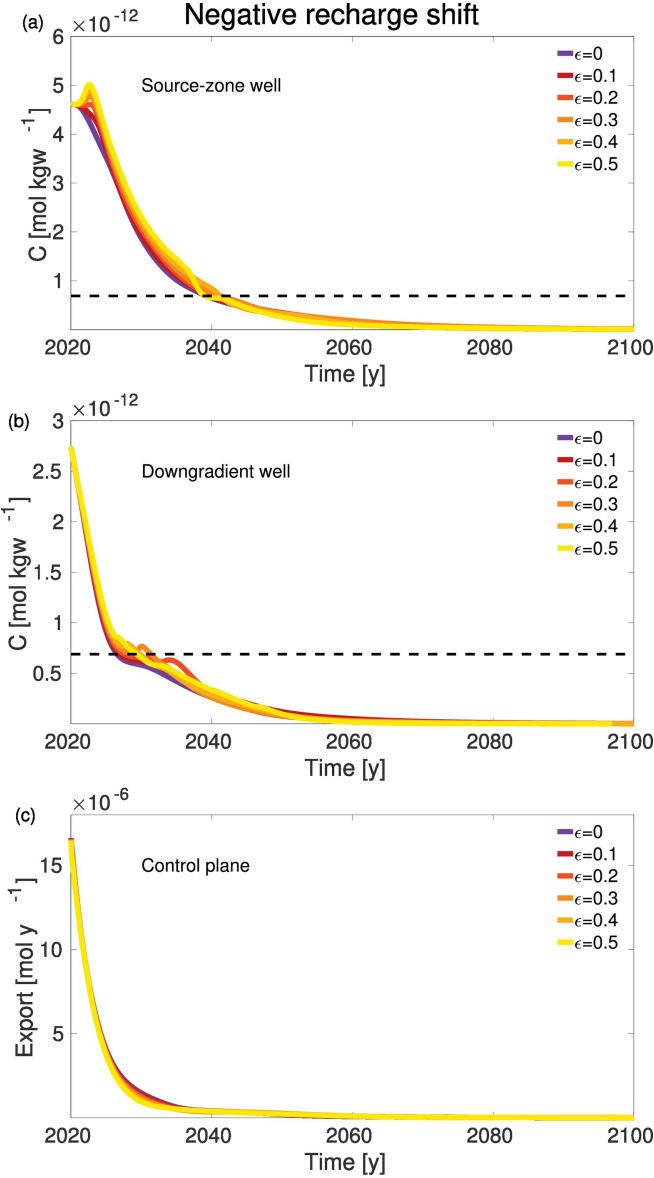
Negative recharge shift
(a)
×10^-12
Source-zone well
C [mol kgw^-1]
Time [y]
(b)
×10^-12
Downgradient well
C [mol kgw^-1]
Time [y]
(c)
×10^-6
Control plane
Export [mol y^-1]
Time [y]
ϵ=0
ϵ=0.1
ϵ=0.2
ϵ=0.3
ϵ=0.4
ϵ=0.5

Figure 7

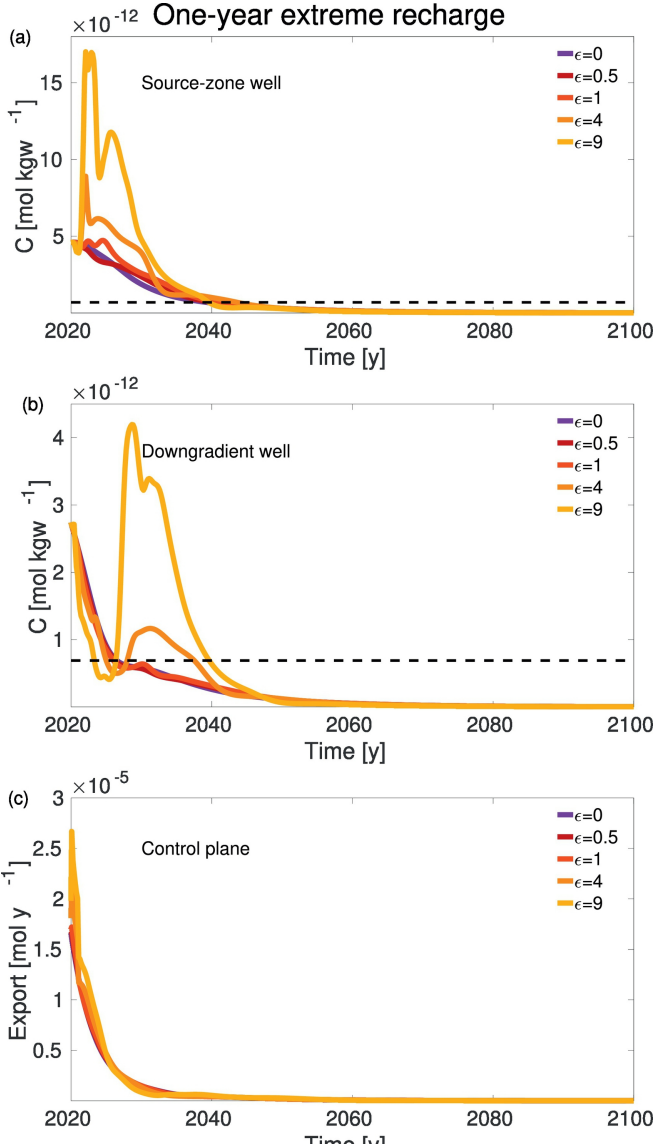
One-year extreme recharge
(a)
×10^-12
Source-zone well
C [mol kgw^-1]
ϵ=0
ϵ=0.5
ϵ=1
ϵ=4
ϵ=9
Time [y]
(b)
×10^-12
Downgradient well
C [mol kgw^-1]
(c)
×10^-5
Control plane
Export [mol y^-1]
2020
2040
2060
2080
2100

Figure 8

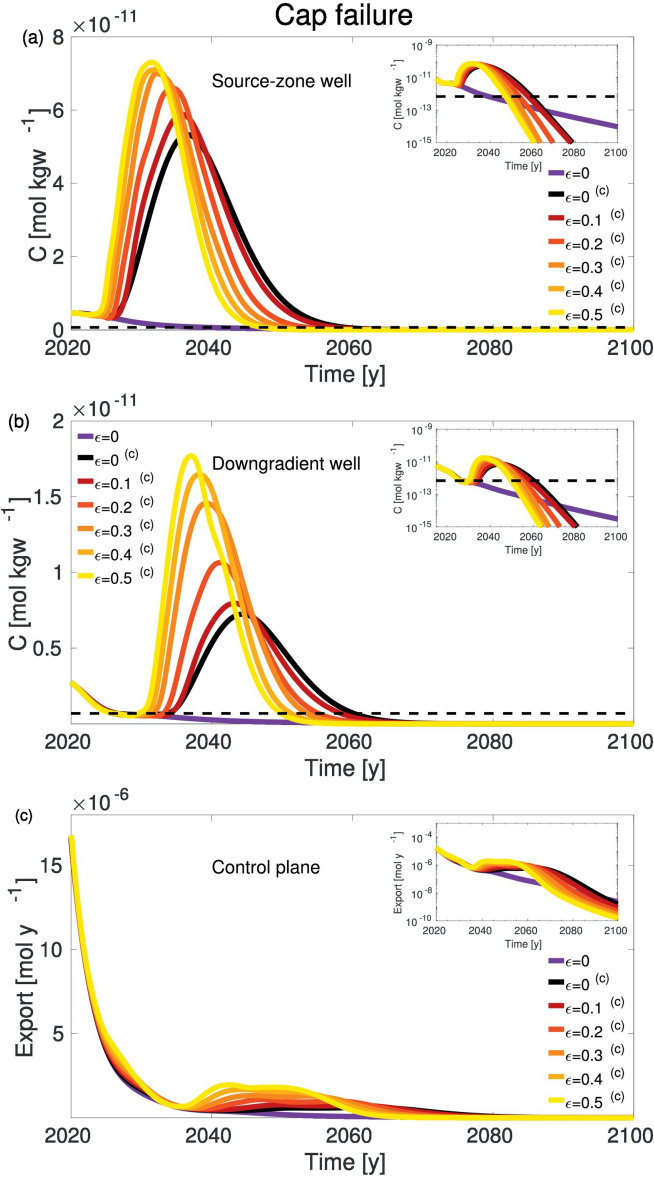
Cap failure
(a)
×10^-11
Source-zone well
C [mol kgw^-1]
Time [y]
(b)
×10^-11
Downgradient well
C [mol kgw^-1]
Time [y]
(c)
×10^-6
Control plane
Export [mol y^-1]
Time [y]
ϵ=0
ϵ=0 (c)
ϵ=0.1 (c)
ϵ=0.2 (c)
ϵ=0.3 (c)
ϵ=0.4 (c)
ϵ=0.5 (c)

Figure 9

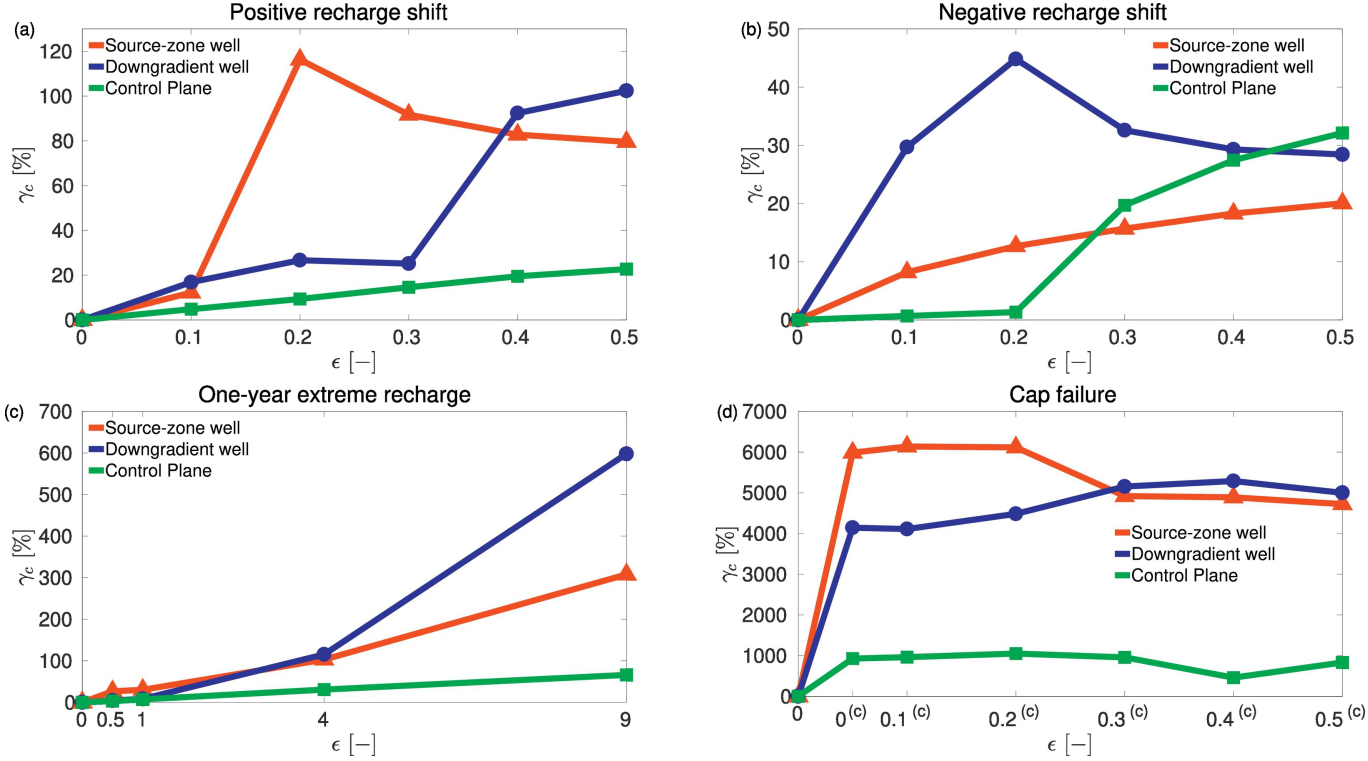
(a)
Positive recharge shift
Source-zone well
Downgradient well
Control Plane
γ_c [%]
ϵ [−]
(b)
Negative recharge shift
Source-zone well
Downgradient well
Control Plane
γ_c [%]
ϵ [−]
(c)
One-year extreme recharge
Source-zone well
Downgradient well
Control Plane
γ_c [%]
ϵ [−]
(d)
Cap failure
Source-zone well
Downgradient well
Control Plane
γ_c [%]
ϵ [−]

Figure 10

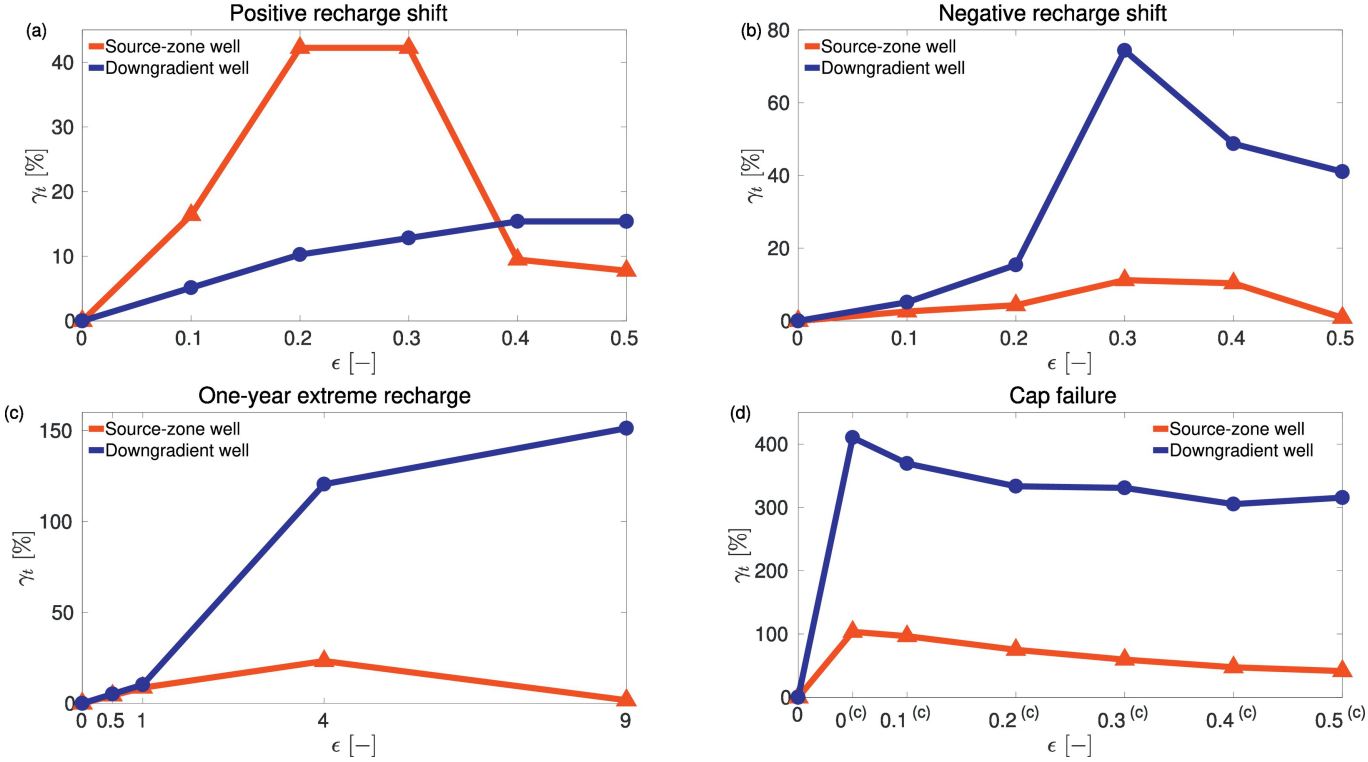
(a)
Positive recharge shift
Source-zone well
Downgradient well
γ_t [%]
ϵ [−]
(b)
Negative recharge shift
Source-zone well
Downgradient well
γ_t [%]
ϵ [−]
(c)
One-year extreme recharge
Source-zone well
Downgradient well
γ_t [%]
ϵ [−]
(d)
Cap failure
Source-zone well
Downgradient well
γ_t [%]
ϵ [−]

Figure 11